Charge carriers injection in tandem semiconductors for dyes mineralization

Alexandru Enesca *, Luminita Isac, Anca Duta

Renewable Energy System and Recycling Centre, R&D Institute of the Transilvania University of Brasov, Eroilor 29 Street, 500036 Brasov, Romania

ARTICLE INFO

ABSTRACT

Four mono-component and three tandem structures were prepared by robotic spray pyrolysis deposition using different precursor compositions and deposition temperatures. The structures of the electronic bands and the light generation/injection of the charge carriers trough the tandem layers (Cu_xS, CuO, SnO_2, ZnO, TiO_2) were studied using electrical (J–V, photocurrent) and optical (UV–vis transmittance) measurements. The crystalline structures and crystallite sizes were evaluated by X-ray diffraction and the morphologies were studied via atomic force microscopy. The wettability properties and the surface energy were calculated based on contact angle measurements using two liquids with different polarities (glycerol and ethylene glycol). The photocatalytic investigations show that the sample containing TiO_2–CuO–Cu_xS–SnO_2 has the highest photo-mineralization efficiency (78% removal of total organic carbon). It was found that copper sulfide compounds increase the photosensitivity properties of the tandem structure especially in vis region of the spectra. The efficiency and kinetics data of the photocatalytic processes were in agreement with the electronic bands alignment, which shows that tandem structures with suitable band energy values and at least one active interface allow high charge carrier mobility and the generation of oxidative species during photocatalysis.

© 2014 Elsevier B.V. All rights reserved.

1. Introduction

The advanced treatment of wastewaters with complex organic pollutants load resulted in industrial processes (especially textile industry) becomes a major issue for all scientific and technological research groups. Even if the traditional techniques for wastewaters treatment are still in use, the advanced oxidations processes (AOPs), based on the generation of reactive species (•OH radicals), are more and more recommended for the oxidative degradation of pollutants, targeting water reuse [1,2]. Wastewater treatment via AOPs, using semiconductor nanomaterials as photocatalysts, seems to be the most promising AOP technology, because photoactivated semiconductors can completely mineralize different types of toxic and non-biodegradable pollutants to CO_2, H_2O and mineral acids under mild conditions: room temperature and atmospheric pressure [3,4].

The photocatalytic performances of metal oxide semiconductors such as TiO_2 [5,6], ZnO [7,8] and SnO_2 [9,10] were intensively investigated, while only few studies [11,12] are reported for Cu_xS (x = 1–2). Except copper sulfides, all above mentioned semiconductor photocatalysts have band gaps in the UV region, ($E_g > 3.2$ eV, $\lambda = 387$ nm), limiting the use of sunlight in industrial applications [13,14] and significantly increasing the process costs. Therefore, to develop market acceptable AOP, many studies are focusing on the synthesis of different coupled tandem semiconductors, such as ZnO/TiO_2 [15], WO_3/TiO_2 [16], SnO_2/TiO_2 [17], Cu_xS/TiO_2 [18] and ZnO/Cu_2O [19], aiming at extending the photocatalytic response in the vis spectral region. A common problem of these systems is finding suitable candidates with band energy values that allow high charge carriers mobility, able to generate oxidative species during photocatalysis. One way to increase the photocatalytic activity of a tandem system is to introduce a compound with photosensitive properties in both UV and vis regions.

Therefore, the main purpose of this study is to present an alternative to increase the UV–vis efficiency of a photocatalyst by coupling different semiconductor materials according to their electronic band structures; the aim is to outline the optimal conditions that support the injection of light generated charge carriers (electrons and holes) and suppress their recombination in the photocatalytic material.

The paper presents a detailed investigation on two—(Cu_xS/SnO_2) and multi-component (ZnO/Cu_xS–CuO/SnO_2 and TiO_2/Cu_xS–CuO/SnO_2) thin films tandem structures, obtained by the successive deposition of individual semiconductor layers,

* Corresponding author. Tel.: +40 726680794.
E-mail address: aenesca@unitbv.ro (A. Enesca).

using robotic spray pyrolysis deposition (RSPD). These types of composites/tandem systems are promising materials for pollutants degradation under UV–vis light irradiation inducing a synergistic effect on charge separation [20]. The use of binary and ternary systems is expected to increase the solar radiation (UV + vis) absorption, by facilitating the charge carrier mobility with positive consequences in photocatalytic reactions. The combinations between the cooper compounds and the metal oxides were selected based on the compatibility between the crystalline structures and the suitable position of the energy bands. Further on, this study demonstrates the influence of composition, crystalline structure and morphology of the individual layers on the interfaces and, consequently on the opto-electrical and photocatalytic properties of the tandem systems.

2. Experimental procedure

2.1. Precursor preparation and deposition parameters

Seven samples were prepared by RSPD using microscopic glass (Heinz Herenz) as substrate for thin films deposition [21]; a set of samples were simultaneously deposited on FTO (fluorine doped tin oxide, F:SnO$_2$, coated glass—Libbey Owens Ford TEC 20/2.5 nm) for the opto-electric analyses. Samples of $2 \times 2 \, cm^2$ substrate were cleaned by successive immersion in ethanol and acetone using an ultrasonic bath.

The precursor solutions for individual metal oxide layers were prepared by mixing tin chloride (SnCl$_4$, 99.99%, Alfa Aesar), titanium chloride (TiCl$_4$, 99.99%, Alfa Aesar) or zinc chloride (ZnCl$_2$, 99.99%, Alfa Aesar) with ethanol (C$_2$H$_5$OH, 99.99%, Alfa Aesar) to form 0.1 M solutions. The precursors solution for Cu$_x$S layers was prepared from 0.3 M copper chloride (CuCl$_2$, 99%, Scharlau) and thioureea (SC(NH$_2$)$_2$, 99%, Scharlau) in 1:3 molar ratio, using as solvent a mixture of water, ethanol and glycerol (C$_3$H$_8$O$_3$, 99.5%, Scharlau) in 7:2:1 volume ratio.

The mechanism of film formation includes: nucleation, formation of the incipient layer and formation of the bulk structure based on aggregates sintering. Previous work [9] showed that the use of inorganic precursors leads to fast nucleation and increases the film uniformity. The number of spraying sequences was 20 for all components but the breaks between two pulses was optimized at: 45 s for tin oxide, 60 s for titanium oxide, 30 s for zinc oxides and 30 s for copper compounds. The carrier gas was air at 1.4 bar and the distance between the spraying nozzle and the substrate was fixed at 15 cm. The abbreviations of the tandem structures consider the metal oxide obtained during the deposition, the layers sequences, the precursors and the deposition temperatures and are presented in Table 1. A schematic representation of the tandem structures is presented in Fig. 1.

After deposition, the samples were annealed at 500 °C for 6 h. The samples containing Cu$_x$S were annealed after the deposition of TiO$_2$ or ZnO as top layer to prevent thermal degradation (oxidation) and sublimation. Due to the thermal instability of Cu$_x$S, the sample Sn_Cu was not annealed.

The deposition and annealing temperatures were optimized in preliminary experiments, based on the stability and polymorphism variation with temperature, and considering the main output property, the efficiency in the dyes photo-mineralization.

2.2. Photocatalysis experiments

The photodegradation reactor consists of a static cylindrical flask, open to air. Combined UV and vis radiation was employed during the photocatalytic experiments by using one F18 W/T8 (black light tubes, UVA, typically 340–400 nm, with $\lambda_{max} = 365$ nm, flux intensity 3 lx, Philips) and two TL-D Super 80 18 W/865 lamps (white cold light tubes, vis, typically 400–700 nm, with $\lambda_{max} = 565$ nm, flux intensity 28 lx, Philips), placed annular to the photoreactor. This combination was chosen as well resembling the solar spectrum (excluding the IR part). In order to prevent light scattering the light sources are circularly positioned around the photocatalytic system. Consequently the radiation is uniformly distributed all over the samples.

The pollutant dye tested in this work was 0.0125 mM methylene blue (99.8%, Merck) prepared by dissolving the powder in ultra-pure water (Direct-Q3 Water Purification System). The photocatalytic degradation of methylene blue was evaluated using a total organic carbon and total nitrogen analyzer (TOC-L + TNM-L, Shimadzu model TOC-LCPH). Experiments used the auto-sample mode at 1 h interval during 6 h.

Before irradiation, each sample ($2 \times 2 \, cm^2$) was inserted in the dye solution into a 25 mL quartz beaker and kept in dark for 1 h to reach the adsorption equilibrium. The changes in concentration were evaluated based on the UV–vis calibration curve, at 665 nm (Perkin Elmer Lambda 950), hourly measured up to 6 h of photocatalysis.

2.3. Thin films characterization

The crystalline structure and the layers composition were evaluated by X-ray diffraction (XRD, Bruker D8 Discover Diffractometer) using the locked-couple technique with 0.002 degree scan step and 0.01 s/step. The surface morphology of the individual and tandem layers was investigated using an atomic force microscope (AFM, NT-MDT model BL222RNTE). The images were taken in semicontact mode with Si-tips (NSG10, force constant 0.15 N/m, tip radius

Table 1
Individual and tandem Cu$_x$S/MO$_x$ layers structures obtained by RSPD.

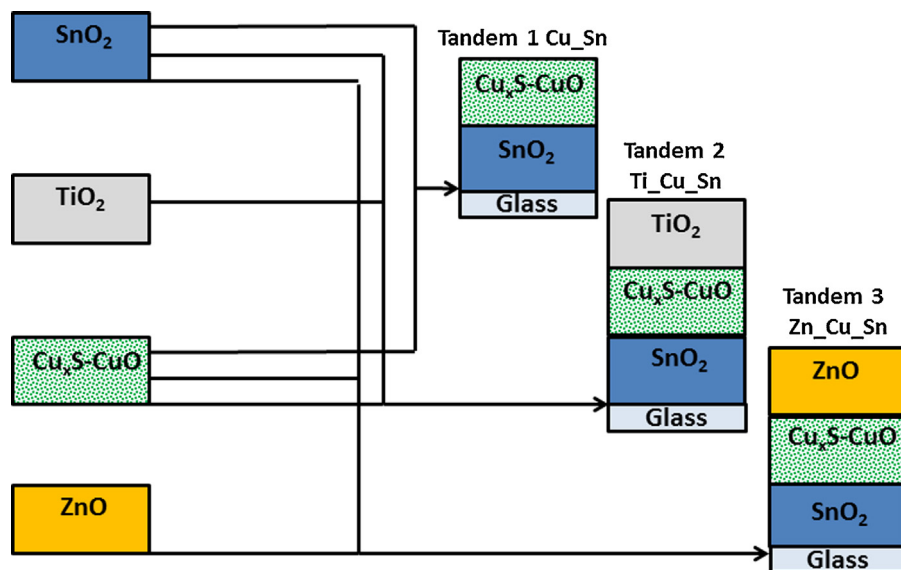| Sample abbreviation	Sample structure	Precursors and deposition temperature for each layer		
		1st layer	2nd layer	3rd layer
Sn	SnO$_2$	**SnO$_2$** SnCl$_4$, C$_2$H$_5$OH; 450 °C	–	–
Zn	ZnO	**ZnO** ZnCl$_2$, C$_2$H$_5$OH; 350 °C	–	–
Ti	TiO$_2$	**TiO$_2$** TiCl$_4$, C$_2$H$_5$OH; 400 °C	–	–
Cu	Cu$_x$S	**Cu$_x$S** CuCl$_2$, SC(NH$_2$)$_2$, C$_2$H$_5$OH, C$_3$H$_8$O$_3$; 300 °C	–	–
Cu_Sn	Cu$_x$S/SnO$_2$	SnO$_2$	Cu$_x$S	–
Ti_Cu_Sn	TiO$_2$/Cu$_x$S/SnO$_2$	SnO$_2$	Cu$_x$S	TiO$_2$
Zn_Cu_Sn	ZnO/Cu$_x$S/SnO$_2$	SnO$_2$	Cu$_x$S	ZnO

Fig. 1. Schematic representation of the tandem structures.

10 nm). Static contact angle measurements with the sessile drop method were recorded and analyzed using an OCA-20 Contact Angle-meter (DataPhysics Instruments). Energy dispersive X-ray (EDS, Thermo) was done to outline the surface elemental composition.

The current–voltage curves and photocurrent measurements used a multichannel potentiostat (PAR Instruments, model HM 8143) with a frequency analyzer, a monochromator (Acton, SpectraPro 2150i) and a UV–vis light source (Oriel, model 7123). The current–voltage analyses were made using two graphite contacts: one contact on the FTO substrate (for applying voltage) and the second on the top of the layers (used as receptor for measuring the current intensity). Both contacts were positioned at equal distance (1.5 cm) on each sample. Optical transmittance measurements were recorded using a UV–vis spectrophotometer (Perkin Elmer Lambda 25 UV/vis).

3. Results and discussions

3.1. Crystalline structures

The XRD analyses (Fig. 2.) show that the two-layered tandems contain chalcocite (Cu$_2$S), as predominant copper sulfide phase (27.93%), with cubic lattice (Table 2) deposited on tetragonal tin oxide (SnO$_2$). The three-layered composites show very weak peaks

of Cu$_7$S$_4$ (roxybite syn) and mainly consist of: (1) hexagonal zinc oxide (ZnO), monoclinic copper oxide (CuO) and tetragonal SnO$_2$, respectively and (2) tetragonal titanium oxide (Ti$_{0.72}$O$_2$, anatase syn), monoclinic CuO and tetragonal SnO$_2$. In these three-component layers, CuO is formed, due to the affinity of Cu^{2+} for oxygen, supported by the high deposition temperature of the top layer: 400 °C for TiO$_2$ and 350 °C for ZnO. An analysis of the JCPDS reference data and of the lattice parameters calculated based on the XRD patterns (Table 2) shows large planar distortion in the ZnO layers (a and b parameters) that can result in stressed structures, with lower stability, thus with a potential larger photocatalytic reactivity. This effect seems to have effect beyond the neighboring layer, as the Zn_Cu_Sn structure shows, with a deviation from the reference lattice parameters registered also for the first layer, SnO$_2$.

The lattice network compatibility between the components of the tandem structures is a pre-requisite for developing strong, uniform and homogeneous interfaces, allowing higher charge carriers mobility [22]. Considering the lattice parameters, CuO compatibility is better supported in the interface with TiO$_2$ than with ZnO.

Interface doping is possible, considering the deposition and the post deposition temperatures along with the similarity in the ionic radii ($r_{Sn^{4+}} = 0.071$ nm, $r_{Cu^{2+}} = 0.072$ nm, $r_{Zn^{2+}} = 0.074$ nm and $r_{Ti^{4+}} = 0.068$ nm) that favors the metal ions diffusion into the neighboring layer(s). However, no evidence of guest ions diffusion into the host lattice is observed from XRD analysis,

Table 2
Crystalline lattices and lattice parameters of the predominant compounds in the tandem structures and JCPDS reference data.

Sample	Crystalline phase(s)	Crystalline lattice(s)	Lattice parameters of the deposited layers		
			a	b	c
	SnO$_2$ tetragonal (JCPDS 01-070-6995)		4.7397	4.7397	3.1877
Cu_Sn	Cu$_2$S/**SnO$_2$**	Cubic/**tetragonal**	4.7373	4.7373	3.1814
Zn_Cu_Sn	ZnO/CuO/**SnO$_2$**	Hexagonal/monoclinic/**tetragonal**	4.7107	4.7107	3.2141
Ti_Cu_Sn	Ti$_{0.72}$O$_2$/CuO/**SnO$_2$**	Tetragonal/monoclinic/**tetragonal**	4.7394	4.7394	3.1766
	Cu$_2$S cubic (JCPDS 00-002-1287)		5.562	5.562	5.562
Cu_Sn	**Cu$_2$S**/SnO$_2$	**Cubic**/tetragonal	5.542	5.542	5.542
	ZnO hexagonal (JCPDS 00-005-0664)		3.249	3.249	5.205
Zn_Cu_Sn	**ZnO**/CuO/SnO$_2$	**Hexagonal**/monoclinic/tetragonal	2.816	2.816	5.207
	Ti$_{0.72}$O$_2$ anatase syn tetragonal (JCPDS 01-086-1157)		3.783	3.783	9.497
Ti_Cu_Sn	**Ti$_{0.72}$O$_2$**/CuO/SnO$_2$	**Tetragonal**/monoclinic/tetragonal	3.787	3.787	9.488
	CuO monoclinic (JCPDS 01-073-6023)		4.6837	3.4226	5.1288
Ti_**Cu**_Sn	Ti$_{0.72}$O$_2$/**CuO**/SnO$_2$	Tetragonal/**monoclinic**/tetragonal	4.6209	3.4150	4.3437
Zn_**Cu**_Sn	ZnO/**CuO**/SnO$_2$	Hexagonal/**monoclinic**/tetragonal	4.6104	3.1505	4.3405

1- SnO2 (JCPDS 01-070-6995)
2- ZnO syn (JCPDS 00-005-0664)
3- TiO2 syn (JCPDS 01-086-1157)
4- CuO (JCPDS 01-073-6023)
5- Cu2S (* JCPDS 00-002-1287, ** 01-072-1071)
6- Cu1.8S (*JCPDS 00-026-0476, ** 00-056-1256)
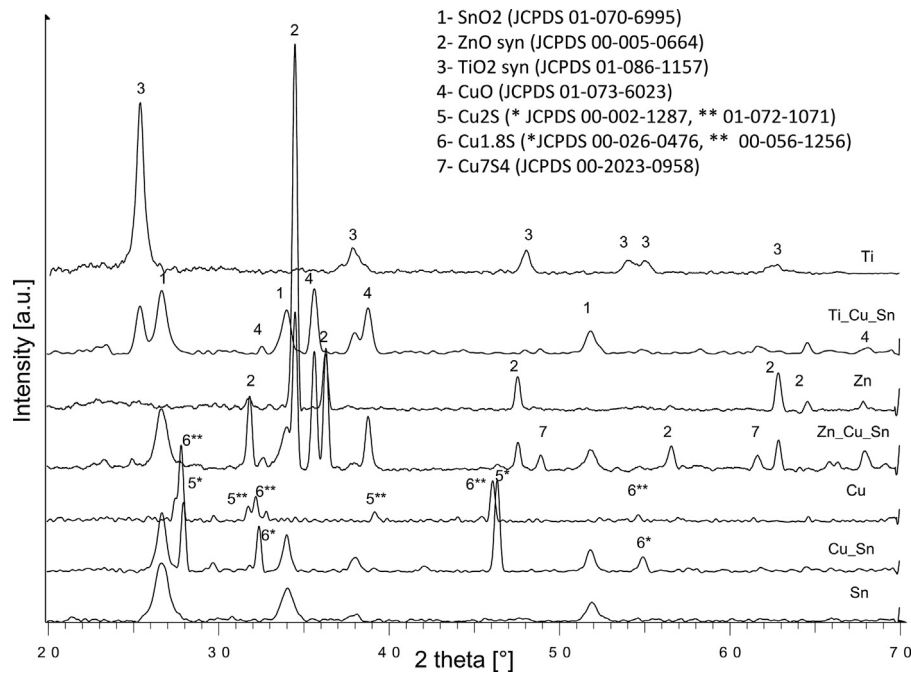7- Cu7S4 (JCPDS 00-2023-0958)

Fig. 2. XRD patterns of individual and tandem layers.

thus no stable crystalline compounds are formed and reciprocal diffusion (if any) is in limited amount.

The crystallites' sizes (Table 3) were calculated using the Scherrer formula according to the diffraction characteristic planes.

$$D = \frac{K\lambda}{\text{FWHM} \times \cos\theta} = \frac{0.9 \times \lambda}{\text{FWHM} \times \cos\theta} \tag{1}$$

The crystallites' sizes (and consequently the aggregates sizes) are directly influenced by the nucleation and crystal growth rates, and by their ratio [23]. The crystallization of ZnO is dominated by the growth process forming large crystallites [24], while TiO$_2$ and SnO$_2$ formation is controlled by nucleation, resulting in much smaller crystallites. The CuO in the multi-component samples is the result of a lattice reaction, showing similar crystallite sizes, with no significant influences of the top layer on the CuO crystal growth, proving a single transformation mechanism.

The substrate also affects the layers formation and this is well confirmed by the variation in the crystallite sizes of each component in the two- and three-layered structures; a combined effect of the crystallinity and morphology on the "substrate" layer can result in smaller crystallites (slow nucleation, e.g. on surfaces rich in edges and corners, as in the case of ZnO) or in larger crystallites on smooth surfaces. Additionally, the longer the residence time on the heated plate, the more significant is the reorganization, with increasing the crystallite size, as proved by the larger values of the SnO$_2$ crystallites in the three-layered structures.

The thickness of the monocomponent was evaluated based on transmittance spectra and refractive index values, and was found to be 280 nm (SnO$_2$), 120 nm (TiO$_2$), 170 nm (ZnO) and 530 nm (Cu$_x$S). During the multi-layers SPD deposition, a densification process is observed as result of a longer residence time on the heater that promotes in situ annealing, with consequences on the chemical composition and crystallinity. A detailed discussion is presented in [25]. Thus the thickness in the mono-component layers represents the maximum thickness value of each specific component in the tandem.

3.2. Morphology and surface tension

The AFM analyses (Fig. 3) shows the formation of granular morphologies of the single metal oxide layers (samples Sn, Zn and Ti) with similar granular size and shape. The lowest roughness value (11.7 nm) corresponds to the Sn sample which also has the smallest aggregates (Table 3).

Sample Cu, containing tetragonal Cu$_2$S and non-stoichiometric cubic Cu$_{1.8}$S, has large aggregates of clustered crystallites, with different shapes and increased roughness (up to 52 nm). When grown on the smooth SnO$_2$ layer, the Cu$_x$S morphology in the binary tandem sample Cu_Sn (Fig. 3e) is significantly different with lower roughness (31.2 nm), showing that morphology can be well controlled by choosing the substrate. The three-component tandem samples exhibit fractal morphology, replicating the initial surface aspect of Cu_Sn and increasing the surface roughness, up to 54.3 nm for Zn_Cu_Sn and 86.8 nm for Ti_Cu_Sn. Higher roughness values and rounded (more stable) morphologies represent an asset in photocatalysis applications which is an interface depended process: large interfaces areas are mostly favorable for obtaining high efficiencies in advanced oxidation processes [26].

The wettability and the surface tension are important parameters for the materials used as photocatalysts in aqueous media [27]. Contact angle measurements (Fig. 4) were used to investigate the influence of the morphology and the crystallinity on the surface energy. Initial contact angles with water were very low (15...20°), proving good surface wettability. But, for accurate measurements, two liquids with different polarities were used: glycerol (with the polar component of the surface energy $\sigma^p = 41.50$ mN/m and the dispersive component of $\sigma^d = 21.20$ mN/m) and ethylene glycol (with the polar component $\sigma^p = 19$ mN/m and the dispersive component $\sigma^d = 29$ mN/m), according to Fowkes [28]:

$$\sigma_{LV}(1 + \cos\theta) = 2\left[\left(\sigma_{LV}^p \sigma_{SV}^p\right)^{1/2} + \left(\sigma_{LV}^d \sigma_{SV}^d\right)^{1/2}\right] \tag{2}$$
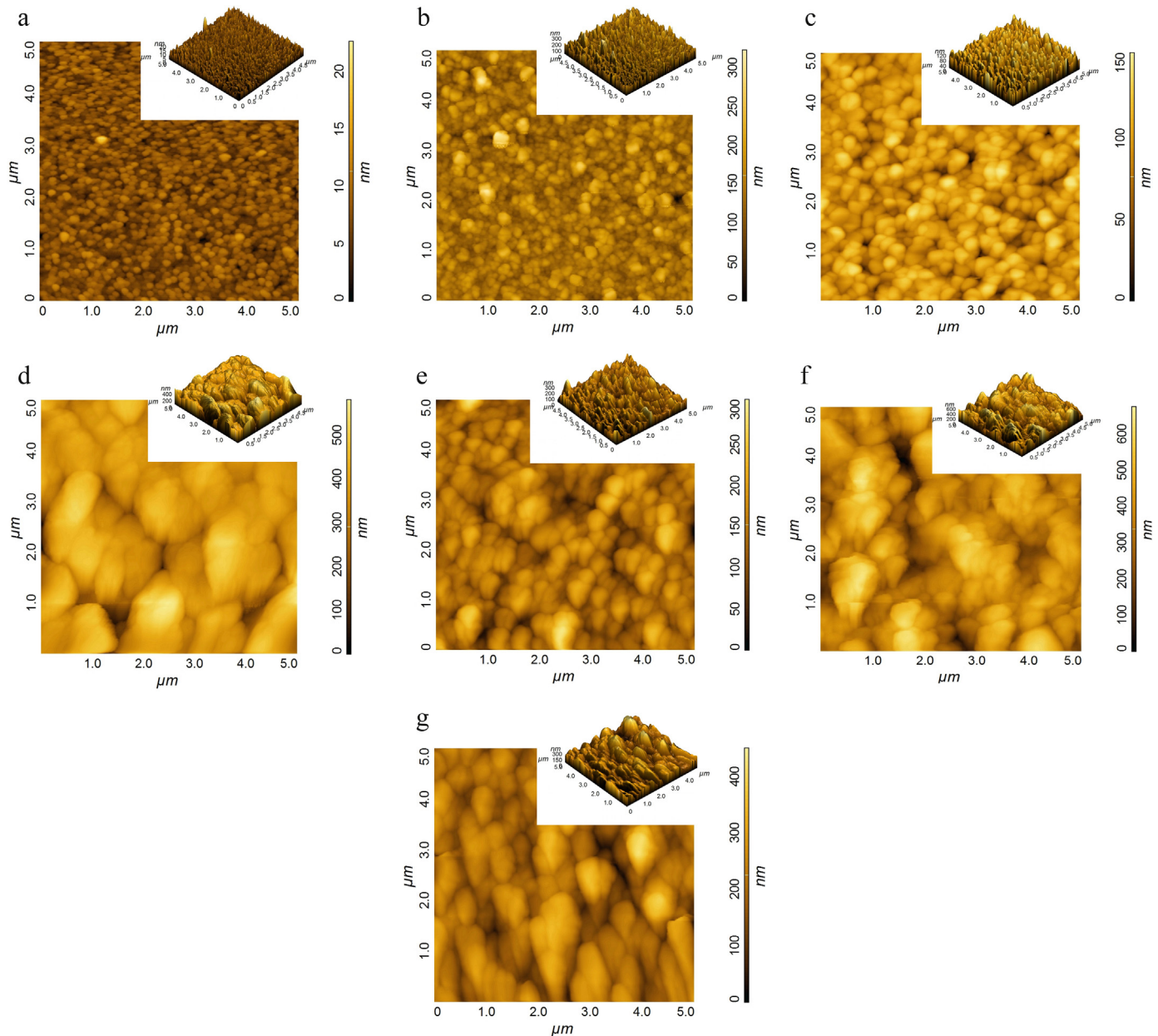
where $\sigma_{LV}^p, \sigma_{SV}^p, \sigma_{LV}^d, \sigma_{SV}^d$ are polar and dispersed components of the liquid- and solid-surface energies, respectively.

The single layered samples, containing large grains with extended boundary interfaces (Sn, Ti, Zn) have the highest energy

Table 3
Crystallite size values calculated using the Scherrer formula and crystalline phase's composition.

Sample	Crystalline phases composition [%]	Crystallite size [Å]					
		SnO_2	ZnO	TiO_2	Cu_2S	$Cu_{1.8}S$	CuO
Sn	SnO_2, 100	82.6	–	–	–	–	–
Zn	ZnO, 100	–	458	–	–	–	–
Ti	$Ti_{0.72}O_2$, 100	–	–	80.7	–	–	–
Cu	$Cu_{1.8}S$, 87.2	–	–	–	280.3	287.8	–
	Cu_2S, 12.8						
Cu_Sn	SnO_2, 62.42	85.3	–	–	339.3	253.9	–
	Cu_2S, 27.93						
	$Cu_{1.8}S$, 9.64						
Ti_Cu_Sn	SnO_2, 50.08	89.1	–	87.4	–	–	266.4
	CuO, 31.66						
	$Ti_{0.72}O_2$, 15.25						
	Cu_7S_4, 3						
Zn_Cu_Sn	ZnO, 44.35	90.9	375.2	–	–	–	256.2
	CuO, 26.8						
	SnO_2, 24.6						
	Cu_7S_4, 4.25						

Fig. 3. AFM 2D and 3D images of: (a) Sn, (b) Ti, (c) Zn, (d) Cu, (e) Cu_Sn, (f) Ti_Cu_Sn and (g) Zn_Cu_Sn.

Table 4
Surface energy components and roughness values.

Sample	Surface energy σ [mN/m]	Dispersive component σ^d [mN/m]	Polar component σ^p [mN/m]	Roughness [nm]
Sn	124.01	10.59	113.42	11.7
Zn	99.13	6.02	93.1	16.5
Ti	85.02	5.43	79.59	27.3
Cu	25.77	23.57	2.20	52.7
Cu_Sn	51.41	47.23	4.18	31.2
Ti_Cu_Sn	51.56	2.90	48.66	86.8
Zn_Cu_Sn	59.42	2.04	57.38	54.3

values. In the multi-layered samples the overall surface energy is almost constant and has significantly different values, as compared to the single-layers. This could be the result of the irregular interpenetration of the thin layers; this assumption is supported by the values corresponding to the contributions of the polar and dispersive components to the total value of the surface energy (Table 4) that mostly depend on the chemical composition of the top layer [29]: when the top layer is a metal oxide the influence of the polar component is predominant (but lower than in the single metal oxide layer); an opposite result is obtained for the sulfide top layer, with lower ionic degree. High surface energy and a large polar component represent an advantage in photocatalytic application, supporting increased wettability and the adsorption of polar or ionic species.

3.3. Electrical and opto-electrical properties

The band gap (E_g) values were calculated based on transmittance spectra (Fig. 5) for metal oxides and based on absorption spectra for copper sulfide. Measurements were done on the single component samples to support the correct estimation of the energy levels in each material.

The optoelectronic properties fundamentally depend on the values of the energy bands, and were calculated according to the algorithms presented in [30,31]. The method for evaluating the valence band (VB) and conduction band (CB) potentials of the semiconductors uses the following equations:

$$E_{VB} = \chi_{semiconductor} - E_e + 0.5E_g \tag{3}$$

where E_{VB} is the valence band (VB) edge potential, $\chi_{semiconductor}$ is the semiconductor electronegativity, E_e is the energy of free electrons vs. hydrogen, E_g is the band gap energy of the semiconductor (experimentally measured), and E_{CB} can be calculated by:

$$E_{CB} = E_{VB} - E_g \tag{4}$$

The absolute semiconductor electronegativity, $\chi_{semiconductor}$(eV) and the absolute cationic electronegativity, χ_{cation}(eV), can be calculated using Eqs. (5) and (6) where χ_{cation}(P.u.) represents the cationic electronegativity (P.u. Pauling units).

$$\chi_{semiconductor} (eV) = 0.45 \times \chi_{cation} (eV) + 3.36 \tag{5}$$

$$\chi_{cation} (eV) = \frac{\chi_{cation} (P.u) + 0.206}{0.336} \tag{6}$$

Based on these calculations, Fig. 6 shows the band structure of the three tandems. In the multi-layered samples, the actual band gap values and their position might be shifted; this can also be expected if non-stoichiometric compounds are formed during the successive deposition steps. The extent of this effect will be discussed in connection with the main output property of these materials—their photocatalytic efficiency in UV–vis.

The Cu_Sn sample, consisting of tin oxide and copper sulfide, shows the highest electrical conductivity in the J–V analysis (see Fig. 7a). According to the band energy diagram for Cu_Sn, the electrons from the tin oxide valence band are promoted on the copper sulfide valence band which is the closest energy level. Under light irradiation, electron–hole pairs are created in a semiconductor [32,33] and when developing an n–p interface/junction the pairs generated within the charged space region can be more effectively separated by the electric field. The n-type SnO_2 and the p-type Cu_xS can form such a junction and the efficiency of this mechanism is confirmed by the photocatalysis results. As mentioned in literature [34,35], the shift in the band gaps is quite low in the case of metal oxides junctions if the stoichiometry is preserved (SnO_2, ZnO and TiO_2 from tandem structures). Related to the copper sulfide compounds, a larger variation is possible considering the stoichiometry
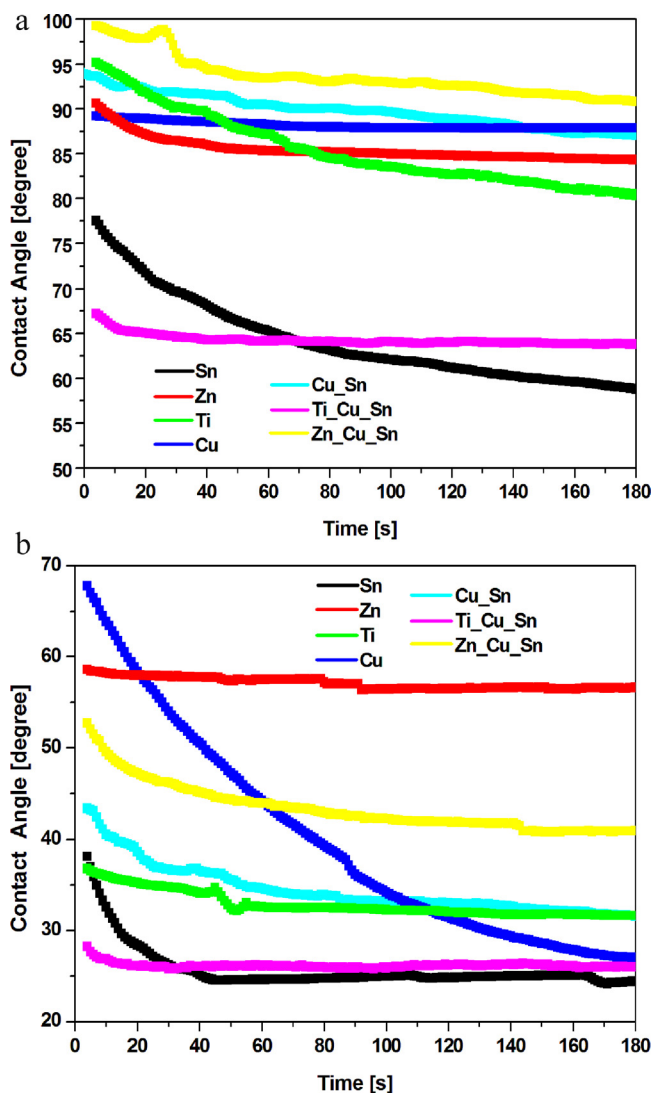
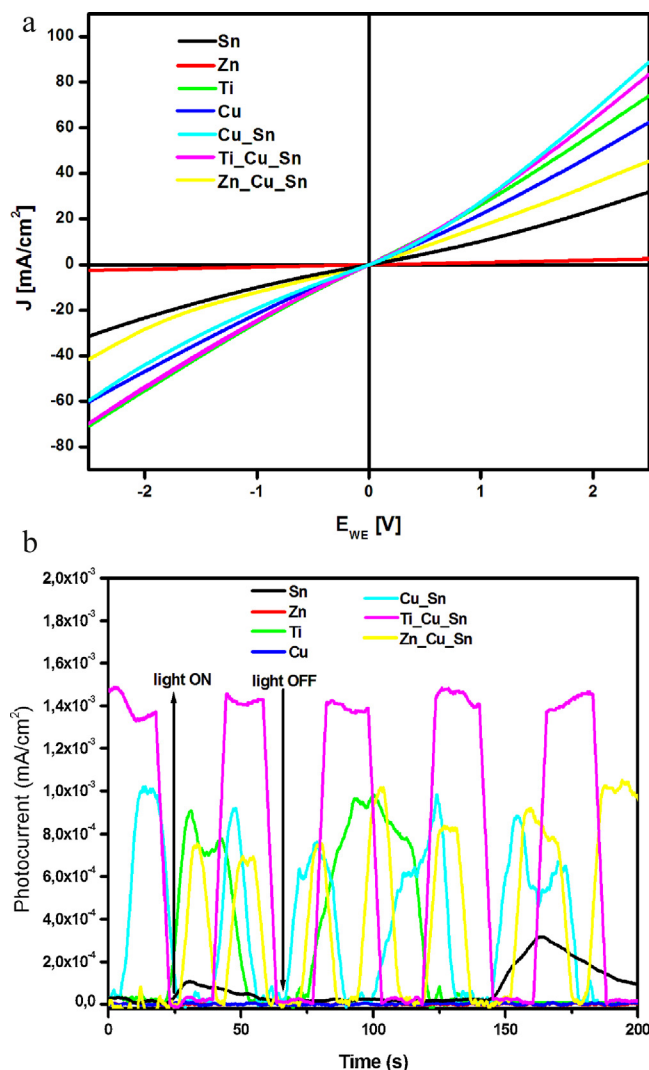**Fig. 4.** Contact angle measurements with (a) glycerol and (b) ethylene glycol.
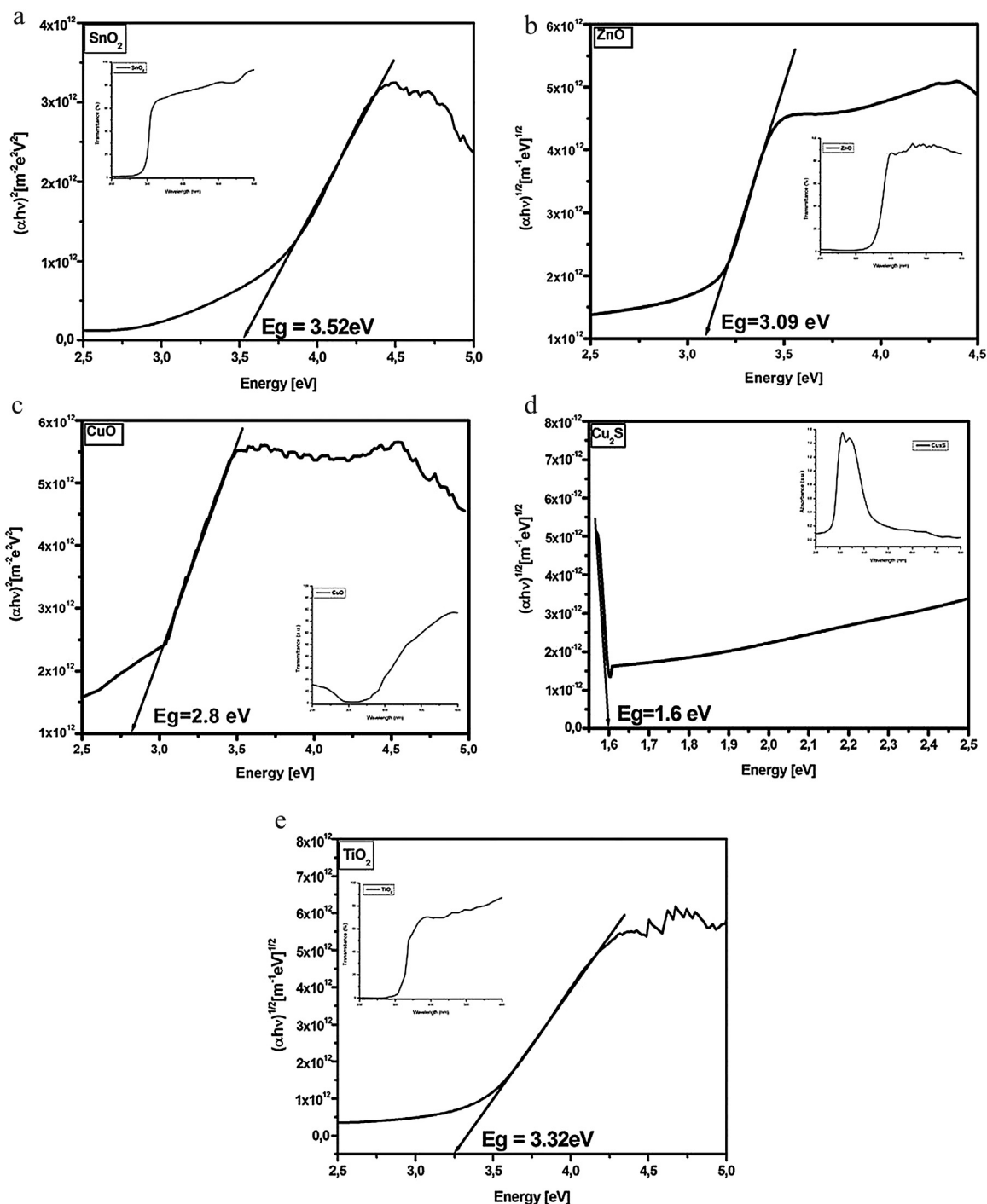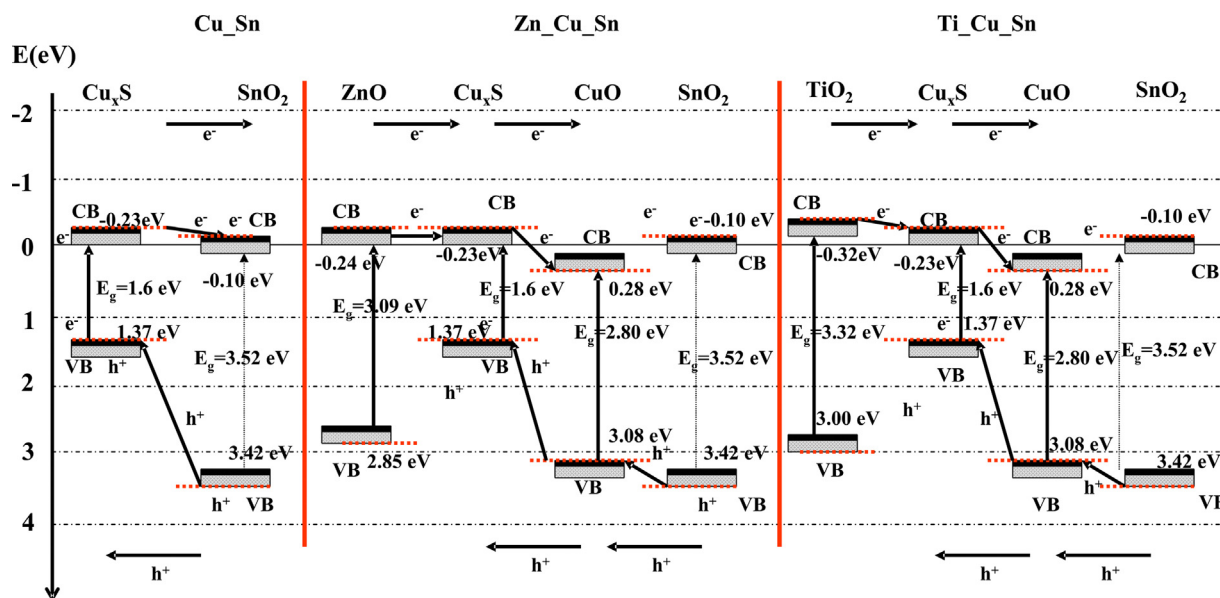
Fig. 5. Band gap estimation based on the transmittance spectra (inset the transmittance spectra) (a) SnO_2, (b) ZnO, (c) CuO, (e) TiO_2 and absorption spectra (inset the absorbance spectra) (d) Cu_2S.

deviations in $Cu_{2-x}S$. However, the influence of this changes are significantly reduced by the low percentage of copper sulfides in the quaternary tandem structures (Table 3): 3% for Ti_Cu_Sn, respectively 4.25% for Zn_Cu_Sn.

By supplementary adding charge carriers (e^- and h^+) in the depletion layer a concentration gradient over the semiconductor is expected, forming a diffuse layer [36]. Therefore, a current will flow due to a combined effect of drift and diffusion by photo-generated electrons. The conduction band (CB) edges of SnO_2 and Cu_xS are conveniently located at −0.23 and −0.10 eV vs. normal hydrogen electrode (NHE). The valence band (VB) edge of SnO_2 (+3.42 eV) is

lower than that of Cu_xS (+1.37 eV). A better charge separation in the coupled film is the result of the fast electron-transfer process from the conduction band of SnO_2 to that of Cu_xS. The charge recombination is suppressed in the coupled film, as compared with the single films and supports the charge carriers' injection trough the layers, thus the formation of oxidative species during the photocatalytic degradation of organic pollutants [37,38].

In the multi-component samples one may consider that CuO and the low amounts of Cu_xS are randomly interpenetrated (3D), leading to dual interfaces with the neighboring layers. As the band structures show (Fig. 6), the multi-stacked layers are relying on

Fig. 6. Energy levels diagram for the bi- and multi-component samples.

Fig. 7. (a) Current density–voltage and (b) photocurrent measurements.

this Cu_xS/CuO interface; active arrangements involve a Cu_xS interface with TiO_2 or ZnO and a CuO interface with SnO_2, allowing the charge carriers flow through two interfaces and giving use to the tandem structure. In the Ti_Cu_Sn sample the TiO_2 conduction band has a higher position than the CB values of Cu_xS, CuO and SnO_2. The charge carriers generation and electrons mobility is mostly favored at the surface and is supported by the homogeneous and uniform interface between TiO_2 and the other layers, as the AFM results showed. In this way the recombination processes are limited, allowing a better mobility of the charge carriers which will be injected in the material(s). This is an advantage for photocatalytic applications as being an interface-dependent process. In the Zn_Cu_Sn sample the ZnO conduction band is very close to that corresponding to Cu_xS and higher than those of CuO and SnO_2. Consequently, this sample will have a lower concentration of charge carriers and a higher electrical resistivity. These results are in good agreement with the XRD data which show the compatibility between the crystalline lattices of the composites in the case of Ti_Cu_Sn sample, supporting the charge carrier mobility.

The bands alignment also show that the three-layered tandems are not involving SnO_2 in the electrons flow, which can also represent and advantage in photocatalysis, when no electron flow/circuit is actually expected but the production of charged species. It can also be expected that very thin films of TiO_2 or ZnO (layer 3) will allow the use of the holes generated in the layers 1 and 2. There are also possible various other mechanisms involving the second, third, etc. layers activated by light penetration, and further work (involving different layers thicknesses) will investigate these assumptions.

These results are confirmed by J–V (Fig. 7a) curves which show lower conductivity for the Zn_Cu_Sn sample as compared to Ti_Cu_Sn. The overall conductivity of the three-component samples is higher than the values exhibited by mono-component samples showing that charge carriers injection occur through the interface(s).

High photosensitivity was observed during photocurrent analysis for the sample Ti_Cu_Sn that reaches the highest saturation of the photogenerated current under UV–vis irradiation. Combining high photosensitive properties with a suitable position of the energy levels can induce an increased charge carrier's concentration, with a positive impact on the photocatalytic activity (formation of the oxidative species). The samples Cu_Sn, Zn_Cu_Sn and Ti
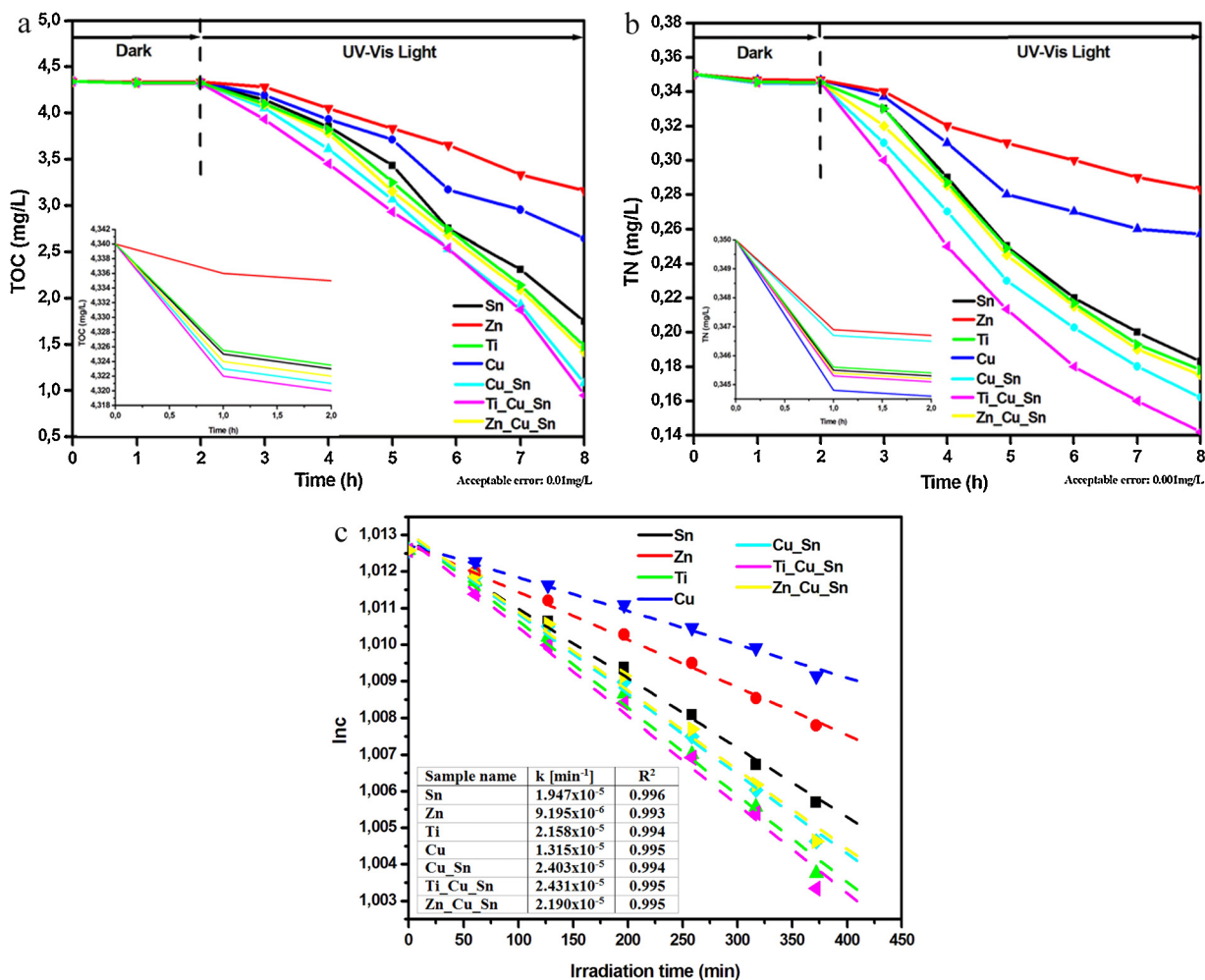
Fig. 8. Photocatalytic activity of the tandem systems (inset: adsorption in dark): (a) total organic carbon (TOC), (b) total nitrogen (TN) and (c) photodegradation kinetics under UV + vis irradiation.

generate lower photocurrent during light irradiation compared with Ti_Cu_Sn sample, outlining the importance of both factors: the alignment of the energy bands and the number of potentially photo-active interfaces. The response time during irradiation is fast (5–10 s) but the photocurrent is not stable as consequence of the interface defects [39,40] and charge carriers recombination [41,42]; the limited recombination induced by the electron traps in TiO$_2$ along with the better CuO/TiO$_2$ interface (as shown in XRD), gives the longest current stability for Ti_Cu_Sn.

Single component structures (the Cu, Zn and Sn samples) are not able to generate enough photocurrent [43] as the amount of UV radiation is low in the experimental conditions, thus they require coupling with other semiconductors (in tandem configuration).

3.4. Photocatalytic activity

The photocatalytic activity of the samples was further investigated. Considering that dyes resulted in the textile industry represent a major pollutant, the photocatalytic experiment was focused on methylene blue (MB) [44,45], a dye showing high chemical stability (heterocyclic aromatic structure inducing a cationic behavior) and recognized passivity to oxidation agents [46,47].

Dyes removal can be done by partial decomposition (bleaching) but this is a rather dangerous path as the by-products may exhibit an even higher pollution risk as the initial compound; therefore total oxidation (mineralization) must be targeted if developing

a process aiming at water reuse. Considering that MB contains both carbon and nitrogen, simultaneous TOC and TN measurements were done. The evolution of the carbon and nitrogen total removal was investigated over 6 h and the data are presented in Fig. 8a and b. Prior to the photocatalytic experiments the samples were immersed in the working solution without irradiation. The measurements show that after 1 h of immersion all samples reach the adsorption equilibrium (inset of Fig. 8a and b).

The initial and current methylene blue concentration was evaluated based on UV–vis absorbance measurements over 6 h and the data were used for kinetic evaluation (Fig. 8c).

The highest photocatalytic activity was observed for the sample Ti_Cu_Sn which shows after 6 h of UV + vis irradiation a total organic carbon removal of 78% (Fig. 8a) and 60% of the total nitrogen (Fig. 8b). This result confirms the contribution of cumulative charge generation (Fig. 9a) while irradiating the tandem structure, with the formation of oxidative species:

$$Photocat + h\upsilon \rightarrow e^- + h^\bullet \tag{7}$$

$$h^\bullet + H_2O\,(Photocat) \rightarrow \bullet OH\,(Photocat) + H^+ \tag{8}$$

As the band structures showed, surface electrons are also likely in these tandems; electrons can be involved in reduction reactions with the photocatalyst. For TiO$_2$ this mechanism involves
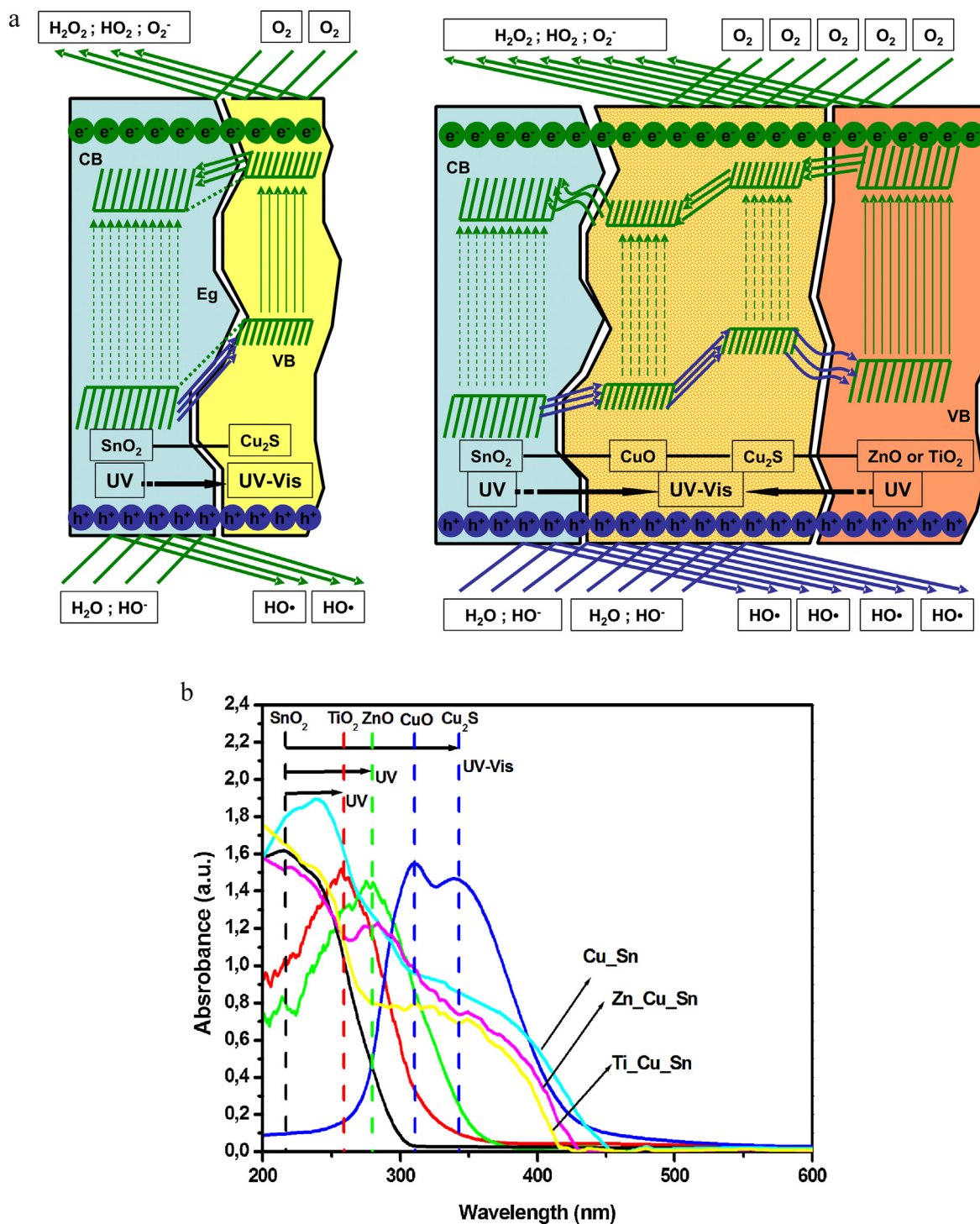
Fig. 9. (a) Charge carrier injection trough the tandem structure and (b) UV–vis absorption spectra corresponding to each layer and tandem structures.

the Ti^{IV}/Ti^{III} reduction (standard reduction potential, $E^0 = -0.092$ V) [48]:

$$e^- + Ti^{IV}OH \rightarrow Ti^{III}OH \tag{9}$$

$$e^- + Ti^{IV} \rightarrow Ti^{III} \tag{10}$$

To investigate the likelihood of these reactions, EDS mapping was done for surface elemental analysis (at%). These data were further used to estimate the maximum oxygen percentage involved in stoichiometric compounds (in their maximum oxidation state) in

the surface depth region accessible to EDS, and most likely accessible to the pollutant dye. The results are presented in Table 5.

Although EDS is not a highly accurate quantitative analysis, the results show a much larger oxygen content at the surface as compared to those that could be involved in stoichiometric compounds, in their maximum oxidation state. Additionally, as the XRD data show, a distinctive peak corresponding to $Ti_{0.72}O_2$, was register (again corresponding to a higher oxygen content than the stoichiometric TiO_2); these can be the results of adsorbed species or surface non-stoichiometry and the possible compounds are likely to undergo reduction for stabilizing their

Table 5
Surface average atomic composition (EDS) and maximum oxygen percentage in stoichiometric compounds.

Sample	Components	Elemental composition [at%]					
		Sn	Ti	Zn	Cu	S	O
Cu_Sn	Cu_xO, CuO, SnO_2	12.2			16.3[*]	6.2	65.3
	Max O % possible	24.4			10.1		34.5
Zn_Cu_Sn	ZnO, Cu_xS, CuO, SnO_2	4.55	–	14.16	7.22[*]	1.39	72.68
	Max O % possible	9.1		14.16	5.83		29.09
Ti_Cu_Sn	TiO_2, Cu_xS, CuO, SnO_2	4.31	12.28	–	7.53[*]	1.25	74.62
	Max O % possible	8.62	24.56		6.28		39.46

[*] Involved in Cu_xS (with $x_{max.} = 1$) and in CuO.

stoichiometry. These reactions, leading to shallow (Eq. (10)) or deep (Eq. (11)) electron traps could prevent recombination, leading to an increased production of reactive photocatalytic species.

For ZnO these reactions are less likely due to the high stability of the Zn^{2+} cation in reduction reactions ($E^0 = -0.76$ V).

The active species likely to be obtained in the two- and multi-component tandems are presented in Fig. 9a. The absorbance spectra (Fig. 9b) show that the tandem structures which contain both metal oxides and cooper sulfide are able to extend the light sensitivity in the visible region comparing with the metal oxides samples which activate only in UV, as result of their band gap values. Compared to mono-component samples, the tandem structures present a shift induced by the metal oxide layer which partially filters the absorbed light. The presence of TiO_2 in the Ti_Cu_Sn sample will reduce the maximum absorption wavelength at 415 nm and in the case of ZnO in Zn_Cu_Sn sample the maximum wavelength reaches 420 nm. As expected, the Cu_Sn sample, which has no metal oxide on the top, has a better vis-absorption; however copper sulfide shows fast degradation during the photocatalytic reaction in wastewater treatment and adding a protective coating is required [49,50].

These results also may support the assumption of a slight shift in the energy band position, particularly at the Cu_xS–CuO–SnO_2 interface, where a 0.38 eV change in the CB position would activate the interface, allowing a longer path of the charge carriers.

By replacing the TiO_2 with ZnO the photocatalytic activity decreases, as expected considering the opto-electric results. The two-component Cu_Sn sample also shows good photocatalytic efficiency, with a total carbon removal of 75% and 54% of the total nitrogen. The mono-component samples have lower photocatalytic activity excepting TiO_2 which is known as highly photosensitive [51,52] and chemically stable [53,54].

The kinetic model for the MB degradation in low concentrated solutions is based on the Langmuir–Hinshelwood (L–H) equation [55,56] which appropriately describes the reactivity results and provides the values of the reaction rate constants in heterogeneous photocatalysis. The reaction rate constant (k) for the pseudo-first order kinetics was obtained by plotting $\ln c$ as a function of the irradiation time (Fig. 8c inset). The highest reaction rate constants correspond to the Ti_Cu_Sn and Cu_Sn samples which is in good agreement with the TOC and TN measurement and confirm the contribution of extra-charge carriers generated in the tandem structure to the dye mineralization. Considering that the photocatalytic processes are surface-dependent the Ti_Cu_Sn sample has the advantage of higher roughness (larger surface), combined with quality interfaces and suitable bands alignment. Samples Zn and Cu have lower rate constants due to the reduced generation of the oxidative species during the irradiation.

The significantly higher photocatalytic efficiency of the Ti_Cu_Sn sample in the mineralization reactions, as compared to the Ti sample is the results of the interfaces developed by the metal oxides with Cu_xS, which facilitate the charge carriers flow through two/three/four interfaces. Consequently the number of holes involved in the formation of oxidative species will increase, accelerating the mineralization process and increasing its efficiency.

4. Conclusions

Seven different samples were prepared by RSPD: four mono-component, one two-component and two three-component structures. The samples exhibit well defined crystalline structures with grain sizes that vary from 80 to 340 Å. The sample containing ZnO has large planar distortions inducing multiple scattering and interfacial defects. The granular morphologies are uniform and homogeneous with a maximum roughness of 86.8 nm (sample Ti_Cu_Sn). The surface energy is mainly influenced by the top layer, and has a predominant polar composition, well supporting the adsorption processes of polar or ionic species.

The energy level diagrams show that the multi-component tandem structures have band energy structures which (partially or totally) allow the generation and mobility of charge carriers trough the samples. Sample Ti_Cu_Sn has the highest photocurrent due to the cumulative charge carriers generation under UV and vis irradiation. The formation of continuous interfaces in the tandem structures is supported by the compatibility in the crystalline structures and induces a better charge separation in the coupled films. The photocatalytic investigations indicate a total organic carbon removal of 78% and 60% of the total nitrogen for Ti_Cu_Sn sample which also has the highest reaction rate constant in methylene blue mineralization.

Acknowledgments

References

[1] P.Y. Chan, M.G. El-Din, J.R. Bolto, Water Res. 46 (2012) 5672–5682.
[2] D. Fatta-Kassinos, M.I. Vasquez, K. Kümmerer, Chemosphere 85 (2011) 693–709.
[3] A. Thiam, M. Zhou, E. Brillas, I. Sirés, Appl. Catal., B: Environ. 150–151 (2014) 116–125.
[4] B.A. Wols, C.H.M. Hofman-Caris, Water Res. 46 (2012) 2815–2827.
[5] M. Visa, A. Duta, Chem. Eng. J. 223 (2013) 860–868.
[6] P. Panagiotopoulou, E.E. Karamerou, D.I. Kondarides, Catal. Today 209 (2013) 91–98.
[7] A.N. Ökte, D. Karamanis, Appl. Catal., B: Environ. 142–143 (2013) 538–552.
[8] S. Liu, X. Wang, W. Zhao, K. Wang, H. Sang, Z. He, J. Alloys Compd. 568 (2013) 84–91.
[9] A. Enesca, L. Isac, L. Andronic, D. Perniu, A. Duta, Appl. Catal., B: Environ. 147 (2014) 175–184.
[10] Y.J. Chiang, C.C. Lin, Powder Technol. 246 (2013) 137–143.
[11] J. Santos Cruz, S.A. Mayén Hernández, F. Paraguay Delgado, O. Zelaya Angel, R. Castanedo Pérez, G. Torres Delgado, Int. J. Photoenergy 2013 (2013) (ID 178017).

[12] Z. Guo, Z. Liu, C. Zhou, J. Han, Y. Zhao, Z. Liu, Y. Li, T. Cui, B. Wang, J. Zhang, Appl. Catal., B: Environ. 154–155 (2014) 27–35.
[13] M. Farbod, M. Kajbafvala, Powder Technol. 239 (2013) 434–440.
[14] X. Zhang, X. Liu, C. Fan, Y. Wang, Y. Wang, Z. Liang, Appl. Catal., B: Environ. 132–133 (2013) 332–341.
[15] S.S. Kanmani, K. Ramachandran, Renewable Energy 43 (2012) 149–156.
[16] A. Enesca, A. Duta, Appl. Phys. A 111 (2013) 639–643.
[17] A. Kusior, J. Klich-Kafel, A. Trenczek-Zajac, K. Swierczek, M. Radecka, K. Zakrzewska, J. Eur. Ceram. Soc. 33 (2013) 2285–2290.
[18] Y. Bessekhouad, R. Brahimi, F. Hamdini, M. Trari, J. Photochem. Photobiol., A 248 (2012) 15–23.
[19] C. Xu, L. Cao, G. Su, W. Liu, H. Liu, Y. Yu, X. Qu, J. Hazard. Mater. 176 (2010) 807–813.
[20] C. Liebig, S. Paul, B. Katryniok, C. Guillon, J.L. Couturier, J.L. Dubois, F. Dumeignil, W.F. Hoelderich, Appl. Catal., B: Environ. 132–133 (2013) 170–182.
[21] M. Enescu, A.J. Catalin, Renewable Sustainable Energy 4 (2012) 053126.
[22] M.I. Schimmel, N.R. de Tacconi, K. Rajeshwar, J. Electroanal. Chem. 453 (1998) 187–195.
[23] C. Li, T. Ahmed, M. Ma, T. Edvinsson, J. Zhu, Appl. Catal., B: Environ. 138–139 (2013) 175–183.
[24] K.J. Chen, F.Y. Hung, T.S. Lui, S.P. Chang, W.L. Wang, Appl. Surf. Sci. 273 (2013) 598–602.
[25] M. Dudita, L.M. Manceriu, M. Anastasescu, M. Nicolescu, M. Gartner, A. Duta, Ceram. Int. 40 (2014) 3903–3911.
[26] J.J. Zou, C. Chen, C.J. Liu, Y.P. Zhang, Y. Han, L. Cui, Mater. Lett. 59 (2005) 3437–3440.
[27] K. Nakata, A. Fujishima, J. Photochem. Photobiol., C 13 (2012) 169–189.
[28] D. Exerowa, N.V. Churaev, T. Kolarov, N.E. Esipova, N. Panchev, Z.M. Zorin, Adv. Colloid Interface 104 (2003) 1–24.
[29] H. Wang, C. Wang, J. Fu, G. Gu, Colloids Surf., A: Physicochem. Eng. Aspects 424 (2013) 10–17.
[30] T. Mise, T. Nakada, Thin Solid Films 518 (2010) 5604–5609.
[31] C. Gao, J. Li, Z. Shan, F. Huang, H. Shen, Mater. Chem. Phys. 122 (2010) 183–187.
[32] S.S. Kalanur, Y.J. Hwang, O.S. Joo, J. Colloid Interface Sci. 402 (2013) 94–99.
[33] H. Melhem, P. Simon, J. Wang, C.D. Bin, B. Ratier, Y. Leconte, N. Herlin-Boime, M. Makowska-Janusik, A. Kassiba, J. Bouclé, Sol. Energy Mater. Sol. Cells 117 (2013) 624–631.
[34] J. Li, J.Z. Zhang, Coord. Chem. Rev. 253 (2009) 3015–3041.
[35] M. Long, R. Beranek, W. Cai, H. Kisch, Electrochim. Acta 53 (2008) 4621–4626.
[36] A. Badawi, N. Al-Hosiny, S. Abdallah, S. Negm, H. Talaat, Sol. Energy 88 (2013) 137–143.
[37] Y. Liu, C. Xie, J. Li, T. Zou, D. Zeng, Appl. Catal., A: Gen. 433–434 (2012) 81–87.
[38] F. Riboni, L.G. Bettini, D.W. Bahnemann, E. Selli, Catal. Today 209 (2013) 28–34.
[39] A.K. Seferlis, S.G. Neophytides, Appl. Catal., B: Environ. 132–133 (2013) 543–552.
[40] S. Sönmezoğlu, S. Akın, Sens. Actuators, A: Phys. 199 (2013) 18–23.
[41] L. Cavigli, F. Bogani, A. Vinattieri, L. Cortese, M. Colocci, V. Faso, G. Baldi, Solid State Sci. 12 (2010) 1877–1880.
[42] F. Lenzmann, M. Nanu, O. Kijatkina, A. Belaidi, Thin Solid Films 451–452 (2004) 639–643.
[43] M.F. Abdel-Messih, M.A. Ahmed, A.S. El-Sayed, J. Photochem. Photobiol., A 260 (2013) 1–8.
[44] M. Tichonovas, E. Krugly, V. Racys, R. Hippler, V. Kauneliene, I. Stasiulaitiene, D. Martuzevicius, Chem. Eng. J. 229 (2013) 9–19.
[45] F. Fu, W. Han, B. Tang, M. Hu, Z. Cheng, Chem. Eng. J. 232 (2013) 534–540.
[46] M.A. Ahmed, Emad E. El-Katori, Zarha H. Gharni, J. Alloys Compd. 553 (2013) 19–29.
[47] S.B. Bukallah, M.A. Rauf, S.S. AlAli, Dyes Pigm. 74 (2007) 85–87.
[48] H.H. Mohamed, D.W. Bahnemann, Appl. Catal., B: Environ. 128 (2012) 91–104.
[49] L.L. Duda, A. Bartecki, Hydrometallurgy 8 (1982) 341–354.
[50] X. Zhang, Y. Guo, P. Zhang, Z. Wu, Z. Zhang, Mater. Lett. 64 (2010) 1200–1203.
[51] U.M. Patil, S.B. Kulkarni, P.R. Deshmukh, R.R. Salunkhe, C.D. Lokhande, J. Alloys Compd. 509 (2011) 6196–6199.
[52] L. Li, L. Qinghua, Y. Jie, Z. Zikang, P. Daocheng, W. Zongguang, Mater. Sci. Eng., C: Biol. Sci. 22 (2002) 61–65.
[53] S. Hu, F. Li, Z. Fan, J. Hazard. Mater. 196 (2011) 248–254.
[54] Y. Li, X. Sun, H. Li, S. Wang, Y. Wei, Powder Technol. 194 (2009) 149–152.
[55] A. Cybula, J.B. Priebe, M.M. Pohl, J.W. Sobczak, M. Schneider, A. Zielińska-Jurek, Appl. Catal., B: Environ. 152–153 (2014) 202–211.
[56] K.V. Kumar, K. Porkodi, F. Rocha, Catal. Commun. 9 (2008) 82–84.